

Full Length Article

Fuzzy symbolic convergent cross mapping: A causal coupling measure for EEG signals in disorders of consciousness patients



Tingting Li ^a, Xingwei An ^{a,b,c,*}, Yang Di ^a, Honglin Wang ^a, Yujia Yan ^a, Shuang Liu ^{a,b,c}, Yueqing Dong ^{d,e,*}, Dong Ming ^{a,b,c}

^a Academy of Medical Engineering and Translational Medicine, Tianjin University, 300072, Tianjin, China

^b Haihe Laboratory of Brain-Computer Interaction and Human-Machine Integration, 300000, Tianjin, China

^c State Key Laboratory of Advanced Medical Materials and Devices, Tianjin University, 300072, Tianjin, China

^d Tianjin Jinnan Hospital, Tianjin University, 300000, Tianjin, China

^e Xincheng Hospital of Tianjin University, 300072, Tianjin, China

ARTICLE INFO

Keywords:

Convergent cross mapping
Fuzzy membership function
Functional network connectivity
Disorders of consciousness

ABSTRACT

Accurate and timely diagnosis in disorders of consciousness (DOC) patients remains a core clinical challenge. Electroencephalography (EEG) shows strong potential for detecting physiological biomarkers of consciousness, and brain network analysis serves as an effective technique. Therefore, a robust approach to brain network construction is of great significance. The convergent cross mapping (CCM) is a powerful tool for capturing the coupling relationship between two signals. However, a major drawback of CCM is its sensitivity to noise. To address this problem, we proposed a symbolic method that combines fuzzy membership functions called fuzzy symbolic convergent cross mapping (FuzzSCCM). Through the simulation results, we verified its robustness to noise, sensitivity to coupling, and data length. Building on this coupling measure, we constructed EEG brain networks and validated the approach on real DOC EEG datasets. In patients with DOC, FuzzSCCM identified distinct network features between vegetative state/unresponsive wakefulness syndrome (VS/UWS) and minimally conscious state (MCS). Specifically, compared with the MCS group, the VS group showed greater asymmetry between the left hemisphere and the right hemisphere in the α band, and was relatively less active in the anterior in the θ band. Moreover, our results demonstrate spontaneous transitions between distinct brain network states, suggesting these dynamic reconfigurations may constitute a fundamental mechanism underlying consciousness modulation. These findings provide novel insights into the dynamic neural signatures of DOC, while establishing a potential diagnostic tool.

1. Introduction

Brain injury often results in prolonged disorders of consciousness (DOC), including a vegetative state/unresponsive wakefulness syndrome(VS/UWS) and a minimally conscious state (MCS) (Giacino et al., 2018). Accurate diagnosis is critical for prognosis and treatment. The gold standard for diagnosing patients with DOC is the JFK Coma Recovery Scale-Revised (CRS-R), which enables the clinical assessment of residual visual, auditory, motor, and verbal functions, as well as communication ability and arousal (Giacino et al., 2004). However, patients often experience unexplained behaviors caused by short (seconds to hours) or long-term (days to months) fluctuations in arousal (Kondziella et al., 2016). This affects the accuracy of the clinical examination based

on bedside behavioral assessment. Accordingly, it is estimated that approximately 40% of patients with DOC are misdiagnosed as being in a VS/UWS (Schnakers et al., 2009). A timely and accurate diagnosis can better support clinicians in making informed decisions regarding patient care and rehabilitation (Ballanti et al., 2022).

At the neural level, severe brain injury often leads to widespread structural disconnection and abnormal functional connectivity (FC). This damages the neural infrastructure that supports consciousness and reduces the ability of information to propagate and dynamically emerge throughout the brain (Rizkallah et al., 2019; Toppi et al., 2024). Patients with DOC exhibit disrupted global information processing (i.e., reduced network integration) alongside enhanced local information processing (i.e., increased network segregation) (Rizkallah et al., 2019). Notably,

* Corresponding authors.

E-mail addresses: lt1999@tju.edu.cn (T. Li), anxingwei@tju.edu.cn (X. An), dy_aquarius@tju.edu.cn (Y. Di), honglinwang@tju.edu.cn (H. Wang), 1021235006@tju.edu.cn (Y. Yan), shuangliu@tju.edu.cn (S. Liu), dongyueqing@tju.edu.cn (Y. Dong), richardming@tju.edu.cn (D. Ming).

the integration of large-scale functional brain networks tends to decline progressively with decreasing levels of consciousness (Rizkallah et al., 2019). Consequently, accurately quantifying the coupling relationships between brain regions has become a central research question in recent years (Chen et al., 2019; Gu et al., 2023; Yi et al., 2024).

Electroencephalography (EEG) signals have attracted growing attention due to their high temporal resolution and ease of acquisition (Chennu et al., 2017; Gu et al., 2023; Hao et al., 2023). In particular, EEG connectomes provide a powerful framework for exploring brain connectivity and offer critical insights into the mechanisms underlying cognitive function (Cao et al., 2022; Demertzis et al., 2019; Wang et al., 2022; Zhang & Chen, 2025). Over the past decades, numerous causality and coupling measures have been developed. Among them, Granger causality (GC) (Granger, 1969) has been widely applied, with extensions to various conditions (Dhamala et al., 2008; Geweke, 1982, 1984). Transfer entropy (TE) (Schreiber, 2000) provides another powerful framework, particularly for capturing nonlinear causality. While these approaches can reveal directional coupling, they often rely on assumptions of stationarity and long recordings, and they may struggle to characterize nonlinear dynamics in the EEG. Recently, convergent cross mapping (CCM), a state-space reconstruction approach with relatively low data requirements (Sugihara et al., 2012), has emerged as an attractive alternative for detecting causal influences (Mi & Lin, 2024; Stavroglo et al., 2019).

While CCM has been successfully applied in neuroscience, its sensitivity to observational noise restricts its clinical applicability. Symbolic extensions of CCM improve robustness by transforming continuous signals into symbolic sequences (Gu et al., 2023). But they rely on hard thresholds, and the richness of the patterns is affected by additional parameters. This may obscure weak yet clinically meaningful interactions, particularly in noisy EEG signals. EEG data from patients with DOC are often contaminated by noise and artifacts, further limiting the reliability of these approaches. Therefore, to effectively detect the coupling relationships between EEG electrodes in DOC patients, the method must exhibit robustness to noise and maintain sensitivity in weakly coupled systems. Exploring the coupling relationship of EEG signals of different brain regions is of great significance for understanding the generation of abnormal EEG signals.

Fuzzy membership functions provide a compelling solution, as they replace hard thresholds with membership degrees, thereby enhancing robustness while preserving subtle signal dynamics. Their flexibility has led to increasing adoption in EEG analysis (Abuhasel et al., 2015; Chatterjee et al., 2013; Lazar et al., 2016). Therefore, we aim to develop a coupling measure that can be reliably applied to low signal-to-noise EEG data and subsequently used to construct brain networks. Such a method is expected to enable the exploration of abnormal connectivity patterns in disorders of consciousness and, in the long term, provide an objective and reliable biomarker to assist clinical diagnosis and decision-making.

In this paper, we proposed a fuzzy symbolic extension of CCM, which enabled the construction of robust directed brain networks with improved noise tolerance. To address the limitation that symbolic patterns are highly dependent on parameter selection, we employed the first-order differential to indirectly capture signal variations instead of relying on absolute amplitude values. The main contributions of this work are as follows: (1) We proposed a novel coupling measure to construct robust brain networks. (2) We integrated symbolic dynamics with fuzzy membership functions to enhance the robustness of causality estimation while preserving sensitivity to weak interactions. (3) We demonstrated that FuzzSCCM reveals distinct network patterns distinguishing MCS from VS patients and, combined with Bayesian NMF, provides novel insights into the neural mechanisms underlying DOC. Compared with the traditional CCM-based framework, our approach exhibits superior performance in detecting the group differences.

2. Method

2.1. Convergent cross mapping (CCM)

CCM uses the dynamical systems theory that time-series variables are causally linked if they share a common attractor manifold to identify the state between variables (Sugihara et al., 2012). A time series is defined as a sequence of data points indexed in temporal order. Considering two time series $\{X\} = \{X(1), X(2), \dots, X(L)\}$ and $\{Y\} = \{Y(1), Y(2), \dots, Y(L)\}$, the central concept of the CCM is whether the present or future value of Y is reliably predicted by reconstructed manifold M_X . The M_X is composed of E -dimensional lagged-coordinate vectors: $X'(t) = \langle X(t), X(t-\tau), \dots, X(t-(E-1)\tau) \rangle$ for $t = 1 + (E-1)\tau$ to $t = L$ (Gu et al., 2023), where the time lag τ is positive and E is the embedding dimensions.

Step 1: We first construct the attractors M_X and M_Y . For a given $X(t)$, we compute the distance between $X'(t)$ and other vectors in M_X . In this paper, Euclidean distance is used. Each vector of M_X is an E -dimensional lagged-coordinate vector.

$$D_X(t) = \{d(X'(t), X'(j)) | j \neq t\} \quad (1)$$

Step 2: Determine the $E+1$ nearest points to $X(t)$ according to $D_X(t)$, and sort their time indices in ascending sequence: t_1, t_2, \dots, t_{E+1} (Mi & Lin, 2024). These $E+1$ vectors form $N_{X'(t)}$.

$$N_{X'(t)} = \operatorname{argmin}_{E+1} D_X(t) = \{X'(t_1), X'(t_2), \dots, X'(t_{E+1})\} \quad (2)$$

Step 3: Compute $Y(t)$ as the weighted mean of the $E+1$ corresponding $Y'(t)$ values (Mi & Lin, 2024).

$$w_i = \exp(-d(X'(t), X'(t_i))/d(X'(t), X'(t_1))) \quad (3)$$

$$\hat{Y}|M_X = \sum w_i Y'(t_i) \quad i = 1, 2, \dots, E+1 \quad (4)$$

Step 4: Follow the above steps, and $\hat{X}|M_Y$ can be calculated.

$$\hat{X}|M_Y = \sum w_i X'(t'_i) \quad i = 1, 2, \dots, E+1 \quad (5)$$

t'_i is calculated from $N_{Y'(t)}$, the details can be found in the above steps.

Step 5: Finally, the Pearson correlation coefficient between the real value and the estimated value is calculated to measure the causal relationship.

$$CCM_{X \rightarrow Y} = PCC(\hat{X}(t)|M_Y, X(t)) \quad (6)$$

$$CCM_{Y \rightarrow X} = PCC(\hat{Y}(t)|M_X, Y(t)) \quad (7)$$

2.2. Fuzzy symbolic convergent cross mapping (FuzzSCCM)

Gu et al. (2023) proposed a dispersive pattern-based symbolization method, which relies on class c and the round operation. As mentioned in the reference Gu et al. (2023), the number of dispersion patterns is c^E , where the value of c determines the complexity of the patterns. To mitigate the influence of c and divide patterns according to the fluctuations in the data, we use the first-order differential of the time series to define classes. The first-order differential emphasizes relative changes rather than absolute amplitudes, thereby reducing susceptibility to noise in data and avoiding the parameter dependence of dispersion-based methods.

$$f_s = \begin{cases} -, \Delta x < 0 \\ 0, \Delta x = 0 \\ +, \Delta x > 0 \end{cases} \quad (8)$$

For a given $X'(t) = \langle X(t), X(t-\tau), \dots, X(t-(E-1)\tau) \rangle$, we first calculate its $(E-1)$ -dimensional first-order difference as $\tilde{X}(t) = \langle (X(t-\tau) - X(t)), (X(t-2\tau) - X(t-\tau)), \dots, (X(t-(E-1)\tau) - X(t-(E-2)\tau)) \rangle$. The sign of each element in $\tilde{X}(t)$ determines the symbol according to Eq. (8). The total number of possible patterns

is 3^{E-1} . The embedding dimension E determines the richness of the symbolic patterns. A higher embedding dimension can capture more complex temporal dependencies, but also increases computational cost and the risk of overfitting. In previous studies applying symbolic dynamics to EEG signals (King et al., 2013), an embedding dimension of $E = 3$ has been commonly adopted. We set $E = 3$ in our experiments. So there are totally $3^2 = 9$ patterns (p_1, p_2, \dots, p_9), the corresponding patterns are as follows:

$$\text{Pattern}(\tilde{X}(t)) = \begin{cases} ++, \Delta x_1 > 0 \text{ and } \Delta x_2 > 0 \\ +-, \Delta x_1 > 0 \text{ and } \Delta x_2 < 0 \\ +0, \Delta x_1 > 0 \text{ and } \Delta x_2 = 0 \\ -+, \Delta x_1 < 0 \text{ and } \Delta x_2 > 0 \\ --, \Delta x_1 < 0 \text{ and } \Delta x_2 < 0 \\ -0, \Delta x_1 < 0 \text{ and } \Delta x_2 = 0 \\ 0+, \Delta x_1 = 0 \text{ and } \Delta x_2 > 0 \\ 0-, \Delta x_1 = 0 \text{ and } \Delta x_2 < 0 \\ 00, \Delta x_1 = 0 \text{ and } \Delta x_2 = 0 \end{cases} \quad (9)$$

where $\Delta x_1 = X(t-1) - X(t)$, $\Delta x_2 = X(t-2) - X(t-1)$. A positive differential ($\Delta x_i > 0$) indicates that the signal is increasing at that time point, whereas a negative differential ($\Delta x_i < 0$) indicates that the signal is decreasing. $\{-, 0, +\}$ corresponds to $\{0, 1, 2\}$. Thus, the symbolic patterns are defined as follows: $p_1 = <+, +> = <2, 2>$, $p_2 = <+, -> = <2, 0>$, $p_3 = <+, 0> = <2, 1>$, $p_4 = <-, +> = <0, 2>$, $p_5 = <-, -> = <0, 0>$, $p_6 = <-, 0> = <0, 1>$, $p_7 = <0, +> = <1, 2>$, $p_8 = <0, -> = <1, 0>$, and $p_9 = <0, 0> = <1, 1>$. For a specific $X'(i) = <2, 3, 1>$, the corresponding $\tilde{X}(i) = <1, -2>$, through Eqs. (8)-(9), the pattern is $p_2 = <+, -> = <2, 0>$. After this process, the time series is transformed into a symbolic sequence.

The use of fuzzy membership functions is suggested to assign a membership degree to each number for each class. The FuzzSCCM method is developed based on the CCM framework (Sugihara et al., 2012). Below, we provide a detailed introduction to the methodological flow within the context of the CCM framework. FuzzSCCM for the time series $\{X\} = \{X(1), X(2), \dots, X(L)\}$ with a length of L can be calculated in six steps.

The first four steps are consistent with the first four steps of CCM.

Step 5: Calculate the pattern of $\hat{X}|M_Y$ and $\hat{Y}|M_X$.

$$\text{Pattern}(\hat{X}|M_Y) = \text{fuzz}(f_s(\hat{X}|M_Y)) \quad (10)$$

$$\text{Pattern}(\hat{Y}|M_X) = \text{fuzz}(f_s(\hat{Y}|M_X)) \quad (11)$$

The Gaussian membership function is employed for the three classes defined in the function f_s . This choice was motivated by its desirable smoothness and symmetry, as well as its ability to incorporate the standard deviation of the data to adjust membership degrees. Specifically, we used the standard deviation of the data as a natural scale parameter, ensuring that the threshold adapts to the variability of the underlying signals. The boundary thresholds of the membership functions were set to $\pm k\delta$, where δ is the standard deviation of the signal and k is a proportional coefficient that adjusts the width of the fuzzy transition region. k is a positive number. This design enables data-adaptive scaling of the fuzzy sets, ensuring robustness against noise while preserving sensitivity to meaningful variations. We defined the fuzzy membership function M_c for class c , where $\mu M_c(x)$ denotes the degree of membership of x to the c th class. In addition, a membership function must satisfy four conditions (Rostaghi et al., 2021). The fuzzy functions used in this paper are as follows:

$$\mu M_0(x) = \begin{cases} 1, x \leq -k\delta \\ 1 - \exp(-x^2/\delta), -k\delta < x < k\delta \\ 0, 0 \leq x \end{cases} \quad (12)$$

$$\mu M_1(x) = \begin{cases} 0, x \leq -k\delta \\ \exp(-x^2/\delta), -k\delta < x < k\delta \\ 0, k\delta \leq x \end{cases} \quad (13)$$

$$\mu M_2(x) = \begin{cases} 0, x < 0 \\ 1 - \exp(-x^2/\delta), 0 \leq x < k\delta \\ 1, k\delta \leq x \end{cases} \quad (14)$$

The boundaries between the classes are usually ambiguous when mapping a classified time series in real-time applications (Rostaghi et al., 2021). A smaller k makes the classification highly sensitive to small fluctuations, which may lead to spurious class changes caused by noise. By contrast, increasing the k enhances robustness, as minor perturbations no longer alter the class. However, an excessively large k reduces discriminability, since both signal-related variations and random noise may be assigned similar membership degrees. Therefore, the choice of k involves a trade-off between robustness to noise and sensitivity to meaningful signal variations. In our method, fuzzy processing is primarily applied to values in the vicinity of zero rather than across the entire data distribution. Accordingly, the parameter k is chosen to be relatively small, ensuring that the membership function is sensitive to subtle variations around zero while remaining unaffected by the broader distributional characteristics. The specific choice and evaluation of k are presented in Section 4.3. Combined with the fuzzy membership function, patterns (see Eq. (9)) also have membership degrees. For the given $X'(t)$, its pattern is the weighted sum of nine patterns.

For further illustration, we present the fuzzy pattern calculation for a lagged-coordinate vector $X'(i)$ of the time series $\{X\}$ with $\delta = 0.05$, $E = 3$, $\tau = 1$, $k = 0.5$. As an example, we set $X'(i) = <0.25, 0.251, 0.281>$. Firstly, $\tilde{X}(i) = <0.001, 0.03>$ is obtained. Using Eqs. (12)-(14), the corresponding membership degrees for the classes are computed: $\mu M_0(0.001) = 0$, $\mu M_1(0.001) = 0.99$, $\mu M_2(0.001) = 0.01$; $\mu M_0(0.03) = 0$, $\mu M_1(0.03) = 0$, $\mu M_2(0.03) = 1$. Subsequently, according to Eq. (9), the probabilities of each pattern are derived as follows: $P(p_1) = 0.001$, $P(p_2) = 0$, $P(p_3) = 0$, $P(p_4) = 0$, $P(p_5) = 0$, $P(p_6) = 0$, $P(p_7) = 0.999$, $P(p_8) = 0$, $P(p_9) = 0$. The fuzzy pattern of $X'(i)$ is calculated as follows:

$$\text{Pattern}(X'(i)) = \sum_{j=1}^{j=9} P(p_j)p_j = <1.001, 2> \quad (15)$$

Step 6: Calculate the Pearson correlation coefficient(PCC) between true patterns and estimated patterns.

$$\text{Fuzzscm}_{Y \rightarrow X} = \sum_{t=1+(E-1)\tau}^{t=L} \text{PCC}(\text{Pattern}(\hat{Y}(t)|M_X), \text{Pattern}(Y(t))) \quad (16)$$

$$\text{Fuzzscm}_{X \rightarrow Y} = \sum_{t=1+(E-1)\tau}^{t=L} \text{PCC}(\text{Pattern}(\hat{X}(t)|M_Y), \text{Pattern}(X(t))) \quad (17)$$

The above steps can be found in Fig. 1(a). The main computational bottleneck of our method lies in computing the pairwise Euclidean distance matrices for each EEG channel, which scales as $O(N \times t^2)$. N is the number of the channel, and t is the length of the time window. Other operations, including fuzzy membership calculations and neighbor weighting, scale linearly with t or quadratically with N , and are comparatively less costly.

To complement the theoretical complexity analysis, we empirically evaluated the computational cost of FuzzSCCM under different numbers of EEG channels and time window lengths. The results are summarized in Table 1. All experiments were repeated 5 times, and the average values are given in the table. When the time window length doubled from 1000 to 2000 points, the average runtime increased approximately three times, consistent with the theoretical $O(N \times t^2)$ complexity. The runtime also increased roughly linearly with the number of channels. Therefore, the quadratic dependence on the time window length dominates the runtime.

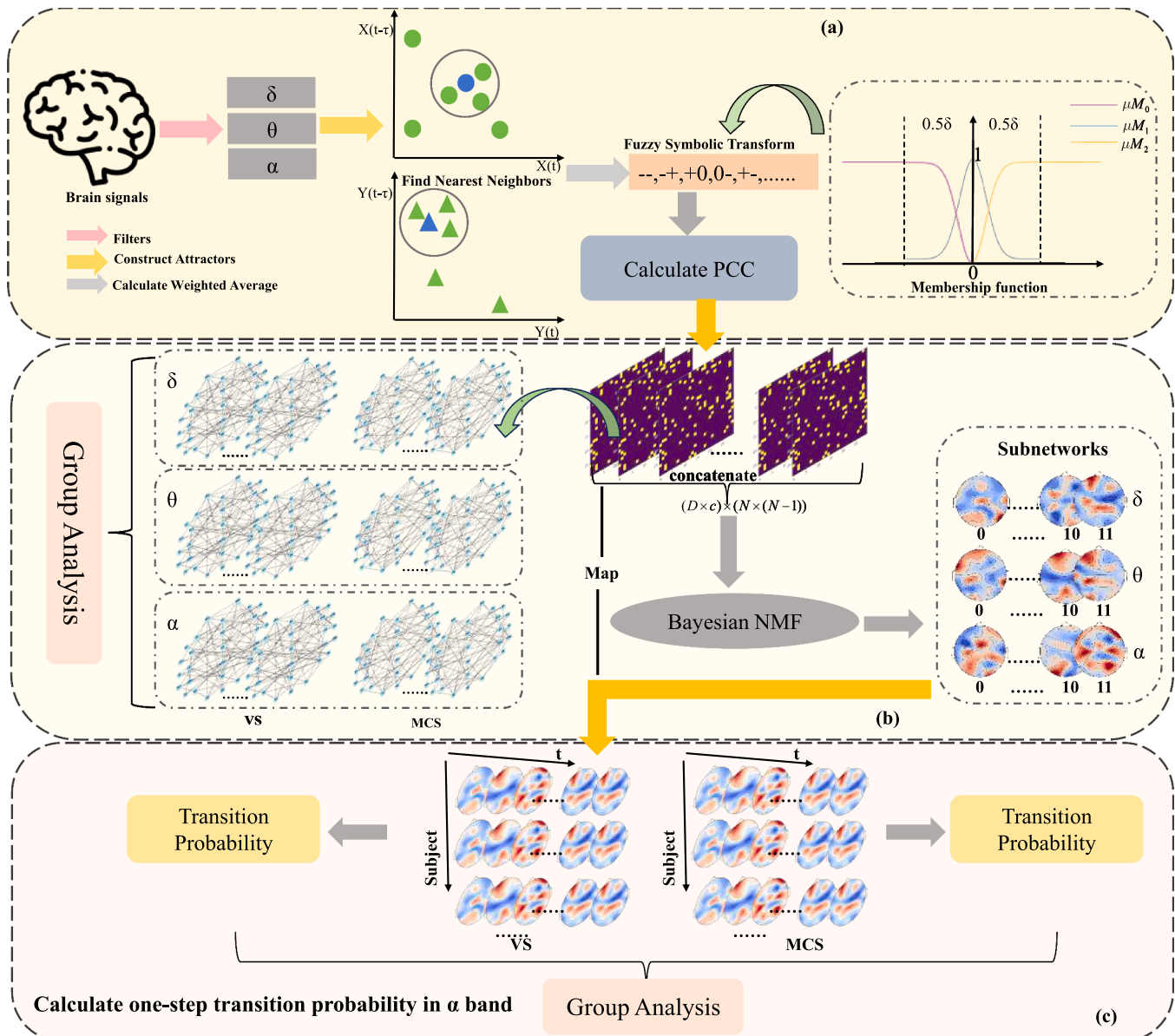


Fig. 1. The workflow for FuzzSCCM and Bayesian NMF-based network analysis. (a) Obtain directed correlations between electrode pairs. (b) Use correlation to construct adjacency matrices and compare static brain network characteristics between the two types of patients. (c) Compare the first-step transition probabilities in brain networks.

Table 1

Empirical runtime of FuzzSCCM under different numbers of channels and time window lengths. All experiments were performed on an Intel i7 CPU (16 GB RAM).

Number of channels (N)	Time window length (t)	Average runtime (s)
16	1000	38
16	2000	113
32	1000	102
32	2000	344

2.3. Construction of directed brain networks

As shown in Fig. 1(b), we used FC to characterize brain networks, where nodes represent electrodes and edges denote connectivity strengths estimated using FuzzSCCM. The adjacency matrix for each subject was obtained by computing FuzzSCCM between electrode pairs in three bands. A cost threshold approach was used to binarize the ad-

jacency matrix (Yi et al., 2022), in which only the strongest connections were retained. Specifically, multiple thresholds (e.g., 10%, 15%, and 20%) were examined, and consistent results across these thresholds confirmed the robustness of our findings. The results obtained under different thresholds are presented in the supplementary material (Figs. S1 and S2). In this study, all brain networks were constructed using a 10% threshold to ensure methodological consistency and comparability across analyses.

2.4. State-specific functional network

In EEG experimental data, electrode coupling is not always stable. To address this, we split the data into segments in chronological order to compute the time-varying causality across the entire sequence. By analyzing functional connectivity across time series spanning different periods, we extend our investigation of brain networks to incorporate dynamic functional connectivity using Bayesian Non-Negative Matrix Factorization (BNMF). As shown in Fig. 1(b), for a given EEG data, a

FC matrix $W \in R_+^{N \times N}$ is generated by FuzzSCCM. N is the number of electrodes. The diagonal elements of the matrix are meaningless. We remove the diagonal elements and flatten it as a vector $V \in R_+^{(N \times (N-1))}$. For each subject, a total of c FC matrices are generated. All individual matrices are vertically stacked to create the aggregated group matrix H , with final dimensions $(D \times c) \times (N \times (N-1))$ where D is the number of subjects.

The NMF can be expressed as $H = AB + E$, where $H \in R_+^{I \times J}$ is the observation matrix, $A \in R_+^{I \times N_{co}}$ and $B \in R_+^{N_{co} \times J}$ (Yi et al., 2020). Here R_+ denotes the set of nonnegative real numbers, $I = D \times c$, $J = N \times (N-1)$, and N_{co} is the number of decomposed components (Yi et al., 2020). Schmidt et al. (2009) used a Bayesian framework to solve this problem, while Yi et al. (2020) applied this method to EEG data. Following their approach, we adopted this method here and set the parameters as specified in the reference Yi et al. (2020). This yields two decomposed matrices, A and B . Each row r in B represents a flattened FC matrix. We then computed the Pearson correlation coefficient between each matrix and each row in B , defining the row with the highest correlation as the State-Specific Functional Network.

2.5. Statistical analysis

To avoid spurious coupling relationships, we generated a set of surrogates data: $\{X'_\sigma | X'_\sigma(t) = X(t+\sigma)\}, \sigma \in \mathbb{N}^+$ (Gu et al., 2023). 50 surrogates were generated by randomizing $\sigma \in [3, 100]$ to create a reference dataset (Gu et al., 2023). Calculate FuzzSCCM values for each set of surrogate data. Then, the coupling relationships were adjusted by retaining only the significantly higher values (permutation test, $p < 0.05$) compared to the reference distribution (Bai et al., 2024). Permutation tests were performed on differences in mean value between $\{FuzzSCCM(X, Y, t)\}_t$ and $\{\cup FuzzSCCM(X'_\sigma, Y, t)\}_t$ (Gu et al., 2023). To ensure sufficient statistical power, a total of 1000 permutation tests were performed.

3. Simulation design

In this study, coupled time series were generated using two Henon map models and a neural mass model. In addition, we performed comparisons with methods based on CCM. The performance of FuzzSCCM was assessed across three key dimensions: noise robustness, coupling sensitivity, and data length sensitivity.

3.1. Henon map model

The Henon map is a classical model widely used for generating chaotic sequences (Mi & Lin, 2024). Many methods (Faes et al., 2011; Lungarella et al., 2007; Vlachos & Kugiumtzis, 2010) often use the model to verify the effectiveness. In our study, we focused on the unidirectional and directional coupling relationship between two series. So, we generated a unidirectionally coupled Henon map model (Chen et al., 2019) and a bidirectionally coupled Henon map model (Mi & Lin, 2024) as follows:

$$\begin{cases} x_t = 1.4 - x_{t-1}^2 + 0.3x_{t-2} \\ y_t = 1.4 - \{ex_{t-1} + (1-e)y_{t-1}\}y_{t-1} + 0.3y_{t-2} \end{cases} \quad (18)$$

$$\begin{cases} x_t = 1.4 - x_{t-1}^2 + 0.1y_{t-2} \\ y_t = 1.4 - \{ex_{t-1} + (1-e)y_{t-1}\}y_{t-1} + 0.3x_{t-2} \end{cases} \quad (19)$$

where the initial values of x and y are randomly chosen between 0 and 1 (Mi & Lin, 2024). $e \in [0, 1]$ is the coupling parameter (Chen et al., 2019).

3.2. Neural mass model

The neural mass model (NMM) (Jansen & Rit, 1995) is a mathematical model used to simulate brain dynamics at the level of neuronal populations. It has proven effective in enhancing our understanding of the characteristics of EEG signals. As a specific type of neural mass model, the Wendling model (David et al., 2004) has been widely employed to investigate the sensitivity of functional connectivity analysis methods (Chen et al., 2019). For two nodes N_1, N_2 , each node is characterized by a parameter w_i . The coupling coefficients C_{21} and C_{12} quantified the strength of connections between N_1 and N_2 . The C_{12} represents the N_1 acting on N_2 and C_{21} represents the N_2 acting on N_1 (Chen et al., 2019). We use the same parameters as in the previous study (David et al., 2004), and the constructed model is unidirectional.

4. Experiment

4.1. Data acquisition

The study protocol was approved by the Ethical Committee of Xincheng Hospital, Tianjin University (approval no. TUXC-2022-R3), and informed consent was obtained from the caregivers of all patients. Patients with DOC were recruited from Xincheng Hospital of Tianjin University between July 2022 and June 2023. All participants were right-handed. Exclusion criteria included pre-existing psychiatric disorders, hearing impairments, intracranial metallic implants (e.g., arterial clips and pacemakers), uncontrollable epilepsy, and involuntary movements. EEG recordings were performed on patients who had not received sedation within the preceding 24 h to minimize the effects of medication on cortical excitability and arousal levels. The final analysis included data from 49 patients with DOC (33 males; mean age: 45.78 ± 13.84 years), comprising 20 recordings from patients in MCS and 29 recordings from patients in VS/UWS. The clinical and demographic characteristics of patients included in the study are presented in Table 2.

All patients were in a resting state, lying on a bed. EEG data were recorded using a 30-channel system (Neuron-Spectrum, Russia). Electrode placement followed the international 10–20 system, with EEG signals referenced to the M1 and M2 electrodes. Electrode impedance was kept below 20 kΩ, and signals were sampled at 500 Hz. Each patient underwent a raw EEG recording lasting 15 to 30 min, conducted by specialist researchers who were blinded to patient information.

Additionally, we included an independent EEG dataset consisting of 47 stroke patients and 34 age-matched healthy controls (dataset details in Yan et al. (2024)). EEG signals were acquired using a quantitative EEG system (Grael EEG, Australia). 32 electrodes were placed according to the international 10–20 system, with the reference set to the average of all electrodes. The recordings were performed by professional technicians who were blinded to patient information. Each EEG session lasted approximately 10–15 min (including preparation).

4.2. Data pre-processing

All EEG recordings in this study were preprocessed using the same semi-automated procedures based on the EEGLAB toolbox (Hao et al.,

Table 2
Demographical and clinical characteristics of the enrolled patients.

N	Age	Gender	Etiology	CRS-R score	Min(age)	Max(age)
MCS	20	48.85±13.96	14M/6F	9E/2A/3S/6T	11.75±2.86	18
VS	29	43.96±13.7	19M/10F	5E/12A/10T/2OT	5.48±1.27	14

S-stroke, T-traumatic, A-anoxic, E-encephalorrhagia, OT-other

Table 3
The channel assigned to the relevant area.

Region	Channel
Anterior	FP2,FP1,F4,FZ,F3,F8,F7,FT8,FC4,FCZ,FC3,FT7
Posterior	TP8,CP4,CPZ,CP3,TP7,T6,T5,P4,PZ,P3,O2,O1
Left	FP1,F3,F7,C3,T3,P3,T5,O1,FT7,FC3,CP3,TP7
Right	FP2,F4,F8,C4,T4,P4,T6,O2,FT8,FC4,CP4,TP8

2023). Data were bandpass filtered from 1 to 30 Hz using a finite impulse response (FIR) filter and then downsampled to 100 Hz. Channels were semi-automatically inspected, and any problematic channels were interpolated. Independent Component Analysis (ICA) was performed using the FastICA algorithm, and artifact-related components (e.g., eye blinks, movements, muscle activities, channel noise, and heart artifacts) were automatically identified and removed using the ICAlabel. Finally, the signal is filtered in the classical EEG frequency band ($\delta(1-4)\text{Hz}$, $\theta(4-8)\text{Hz}$, $\alpha(8-13)\text{Hz}$).

For consistency across patients, we symmetrically discarded the beginning and end segments of each recording and retained the central 5 min of EEG data (Hao et al., 2023). Then, each subject's EEG signal was subsequently segmented into 30 non-overlapping epochs of 1000 samples using a sliding window of 1000 time points with a step size of 1000. After preprocessing, each subject's EEG data in each band was segmented into 30 non-overlapping epochs (1000 samples per epoch). For each epoch, we constructed a functional brain network using FuzzSCCM, resulting in 30 networks per subject in every band. In the static network analysis, the features we calculated are the mean of 30 networks. We split the brain into 4 regions: anterior, posterior, left, and right, according to the location of the electrodes (Mi & Lin, 2024), and the channels for each region are shown in Table 3.

For the stroke dataset, due to differences in recording durations between the two groups, EEG signals from stroke patients were downsampled to 500 Hz, while those from healthy controls were downsampled to 200 Hz. All subsequent preprocessing procedures were performed identically to those applied to the DOC dataset.

4.3. Selection of k

To evaluate the effect of parameter selection, we conducted two sets of empirical analyses. For the Henon model with a unidirectional coupling strength of $e = 0.1$, we used simulated data to investigate the robustness to noise at various k values. Inspired by the study Rostaghi et al. (2021), we use the ratio of the noised value to the original value to verify robustness to noise in simulated data.

$$\text{Ratio} = \frac{\text{measured coupling of a series with noise}}{\text{measured coupling of a series without noise}} \quad (20)$$

A Ratio value closer to 1 indicates lower sensitivity to noise. For the real EEG data, to establish the clinical relevance of hemispheric lateralization, we first examined power spectral density (PSD) features in the α band. The PSD asymmetry is calculated as follows:

$$\text{PSD asymmetry} = \frac{|\sum \text{PSD}_i - \sum \text{PSD}_j|}{\sum \text{PSD}_i + \sum \text{PSD}_j}, i \in \Lambda_{left}, j \in \Lambda_{right} \quad (21)$$

Where Λ_{left} represents the left-hemisphere brain electrodes set, and Λ_{right} represents the right-hemisphere brain electrodes set. The results revealed a significant left-right asymmetry between MCS and VS patients ($p < 0.05$), indicating that hemispheric imbalance is a valid neurophysiological marker in this cohort. The choice of k value was then evaluated by examining whether these network features consistently showed significant differences between the two patient groups. Then, we propose a new metric to assess the degree of lateralization of left and right brain connections.

$$LR = \frac{|\sum C_i - \sum C_j|}{\sum C_i + \sum C_j}, i \in \Lambda_{left}, j \in \Lambda_{right} \quad (22)$$

where C_i denotes the degree of node i . We computed the average LR across 30 brain networks in the α band to evaluate differences between MCS and VS. This analysis aimed to determine whether significant group differences ($p < 0.05$) could be consistently identified regardless of the choice of k . In addition, the Relative Standard Error(RSE) of the mean LR for each group was calculated to evaluate the stability of LR across different k values.

$$RSE = \frac{SE}{\bar{x}} * 100\%, SE = \frac{s}{\sqrt{n}} \quad (23)$$

where s is standard deviation, \bar{x} is mean and n is the number of samples in each group(VS: $n = 29$, MCS: $n = 20$).

As shown in Fig. 2(a), we compared the variation of the *Ratio* with increasing noise levels for $k = 0.1, 0.3, 0.5, 0.7$, and 0.9 on the Henon model. The results indicate that the *Ratio* decreases as noise increases. When $k < 0.5$, the method exhibits higher sensitivity to noise, whereas at $k = 0.5$ a marked improvement in performance is observed. For $k > 0.5$, the *Ratio* approaches 1 and tends to stabilize. Then, we computed the relative standard errors (RSE) of the FuzzSCCM values across different k settings for both the VS and MCS groups, as illustrated in Fig. 2(b).

The results demonstrate that both excessively small and large values of k lead to increased variability, reflected in higher RSE. In contrast, the setting of $k = 0.5$ consistently yielded the lowest RSE, suggesting that this parameter choice provides the most statistically stable and reliable estimation. Although the stability varied with different k values, the significant differences($p < 0.05$) in LR between the two groups remained consistently observable regardless of the choice of k (Fig. 2(c)). Accordingly, $k = 0.5$ was determined to be an appropriate parameter setting and was thus employed in the subsequent analyses.

4.4. Simulation assessments

4.4.1. Results for the Henon map model

To test whether our method is effective in low-coupled systems, we set e to 0.1 in both Eqs. (18) and (19). For each model, we simulated a total of 30 realizations with a length of 1000. Additionally, we superimposed white noise (standard deviation range from 0.1 to 1, step size 0.1) onto the original signal. The results for unidirectional coupling are shown in Fig. 3(a). The findings indicate that under $e = 0.1$, the *Ratio* of all three methods exhibits a downward trend as noise increases.

Among them, FuzzSCCM demonstrated greater stability than SCCM under the same conditions. Although the coupling strength from X to Y is weak, the *Ratio* of FuzzSCCM remains closer to 1. This suggests that the fuzzy membership function effectively reduces sensitivity to noise, particularly in weakly coupled systems. We also compared the three methods using the bidirectional Henon map model. Setting $e = 0.1$ in Eq. (18), we observed in Fig. 3(b) and (c) that FuzzSCCM is also less sensitive to noise. Above all, whether the coupling is unidirectional or bidirectional, FuzzSCCM is more robust.

The coupling strength sensitivity of FuzzSCCM was assessed by varying parameter e in Eq. (18) across three levels (0.1, 0.3, 0.5). We calculated the average and standard deviation of the coupling value from X to Y of the 30 realizations. Fig. 3(d) shows that FuzzSCCM has a smaller standard deviation and a higher measured value. Additionally, the fluctuations of the three methods were generally consistent.

4.4.2. Results for the neural mass model

For the unidirectional NMM model, we aimed to evaluate the strength and length sensitivity of FuzzSCCM by increasing the data length from 1000 to 6000. In this section, we set $C_{21}=0$ and tested coupling sensitivity at 3 levels($C12 = 0.1, C12 = 0.3$ and $C12 = 0.5$). As shown in Fig. 4(left), the FuzzSCCM method exhibits good convergence, with no significant fluctuations in its values as the data length increases. Therefore, FuzzSCCM does not impose excessive requirements on data length. To optimize computational efficiency, we set $L = 1000$ for subsequent EEG data processing. Fig. 4(right) also demonstrated that the

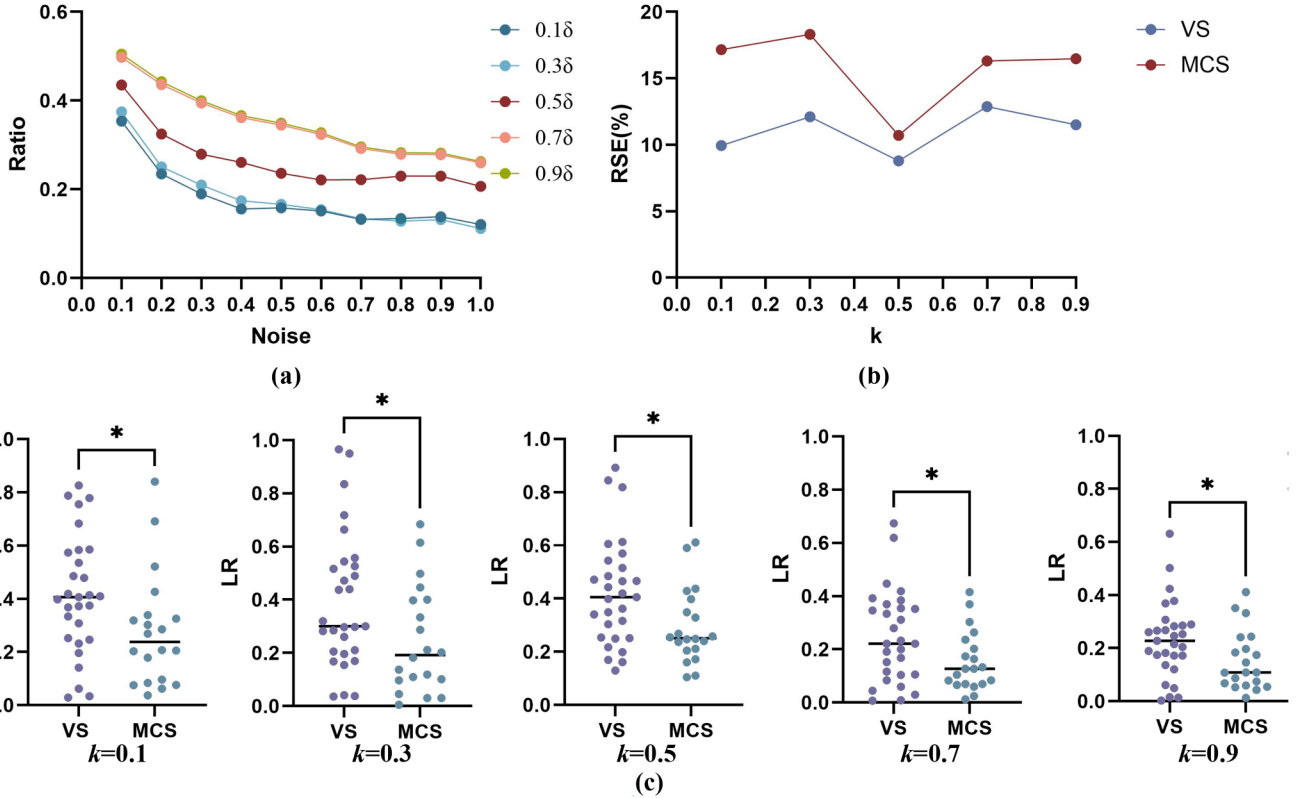


Fig. 2. The results of FuzzSCCM values on simulated data and EEG data at different k values. Among these settings, $k = 0.5$ yields the most stable and reliable performance. (a) The *Ratio* of different k , noise standard deviation from 0.1 to 1 (step size 0.1). (b) The RSE of *LR* for two types of patients at different k values. (c) *LR* values of EEG in MCS and VS in the α band. From left to right, results correspond to $k = 0.1, 0.3, 0.5, 0.7$, and 0.9. Unpaired t-test was performed, * $p < 0.05$.

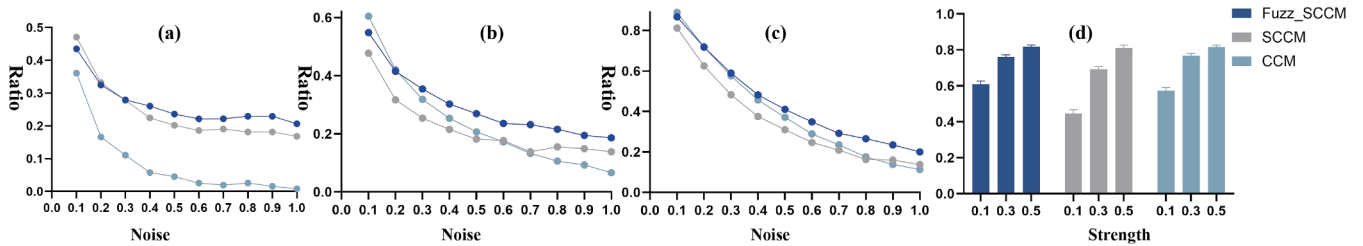


Fig. 3. Comparison of CCM, SCCM, and FuzzSCCM results of Henon map model. (a) Under $e = 0.1$ in Eq. (18), the *Ratio* of all three models, noise standard deviation from 0.1 to 1 (step size 0.1). (b) Under $e = 0.1$ in Eq. (19), the *Ratio* from Y to X of all three models, noise standard deviation from 0.1 to 1 (step size 0.1). (c) Under $e = 0.1$ in Eq. (19), the *Ratio* from X to Y of all three models, noise standard deviation from 0.1 to 1 (step size 0.1). (d) Comparison of unidirectional coupling metrics at three coupling strengths.

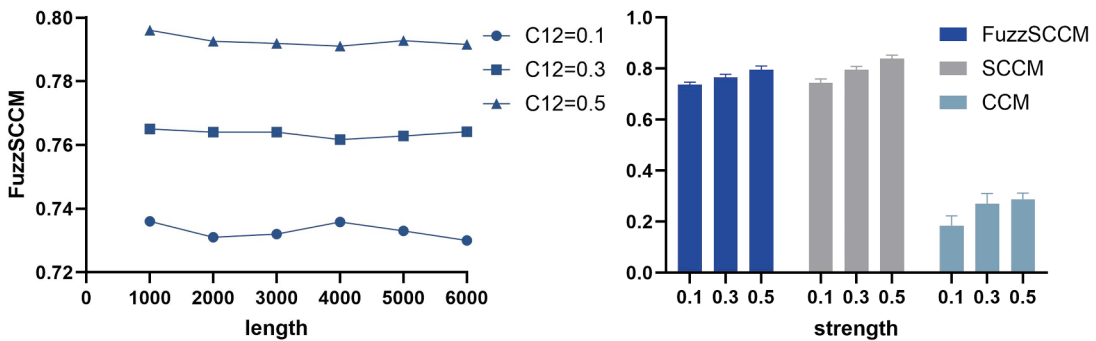


Fig. 4. Performance of FuzzSCCM in the Neural Mass Model (NMM) simulation. (Left) FuzzSCCM values as a function of time series length under three different coupling strengths ($C_{12} = 0.1, 0.3, 0.5$). (Right) Comparison of FuzzSCCM, SCCM, and CCM across different coupling strengths. Error bars denote standard deviations across 30 independent simulations.

three models were sensitive to coupling strength. This may be due to the sensitivity of CCM method.

4.5. Real data application

This study aimed to systematically compare neural coupling patterns between MCS and VS across distinct frequency bands and brain regions. We analyzed the differences between the two patient groups from both static and dynamic perspectives.

4.5.1. Static functional brain network

As shown in Fig. 1(b), we used FC to characterize brain networks, where nodes represent electrodes and edges denote connectivity calculated by FuzzSCCM. For each frequency band, the adjacency matrix for each subject was obtained by computing FuzzSCCM between electrode pairs. A cost threshold approach (keep the top 10% connections in the network) was used to binarize the adjacency matrix (Yi et al., 2022). Notably, the characteristics of time-varying directed networks remained consistent across different thresholds (10%, 15%, and 20%), showing patterns highly similar to those observed at the 10% threshold (Fig. S1 and S2 in the supplementary materials). This reproducibility strongly demonstrates the robustness of the constructed network architecture.

As shown in Fig. 5(a), there was a significant difference between MCS and VS derived from FuzzSCCM in the α band ($p < 0.05$). The LR asymmetry of VS is stronger. From Fig. 5(d), we can see that the relative LR derived from FuzzSCCM in α band and δ band is also significantly different ($p < 0.05$). These findings suggested that the VS group was char-

acterized by a higher LR in a high frequency band and relatively lower in the low frequency band.

To visualize the differences in hemispheric connectivity, we selected one representative patient from each group for comparison. Based on the electrode positions, we calculated the absolute degree difference map by subtracting the degree of each right-hemisphere electrode from its symmetrical counterpart in the left hemisphere and taking the absolute value. From Fig. 6(a), we can find that brain networks constructed using SCCM exhibit little differences in left-right asymmetry between the two patients. In contrast, our method clearly reveals that VS patients display more pronounced hemispheric asymmetry. These results suggest that our method more effectively captures inter-group differences in hemispheric connectivity.

As shown in Fig. 5(c), significant differences ($p < 0.05$) in PSD were observed between the two groups in the α band, with the VS group exhibiting higher values. This suggests that PSD asymmetry in the left and right hemispheres was more pronounced in the VS group. SCCM was used to construct brain networks, and the LR was calculated accordingly. The relative LR in α band and δ band based on SCCM also showed significant differences ($p < 0.05$) between the two groups, as shown in Fig. 5(e). Consistently, our proposed method corroborated these findings, further supporting its validity in capturing clinically relevant hemispheric asymmetry.

Similar to LR , we propose a new metric to evaluate the degree of lateralization of anterior and posterior brain connections.

$$AP = \frac{\sum C_i - \sum C_j}{\sum C_i + \sum C_j}, i \in \Lambda_{\text{anterior}}, j \in \Lambda_{\text{posterior}} \quad (24)$$

where C_i denotes the degree of node i , $\Lambda_{\text{anterior}}$ is the anterior-hemisphere brain electrodes set, and $\Lambda_{\text{posterior}}$ is the posterior-hemisphere brain electrodes set. The result is shown in Fig. 5(g).

4.5.2. Dynamic functional brain network

For AP , significant differences ($p < 0.01$) between VS and MCS were found only in the θ band. In the MCS group, anterior connections were stronger than posterior connections, whereas the opposite trend was observed in VS. We also demonstrated the whole degree distribution of the former two patients; the result is shown in Fig. 6(b). While the SCCM method did not reveal any significant differences, our method clearly showed that anterior connections were more active in MCS patients. Notably, the connectivity between anterior and posterior brain regions in the θ band may serve as a sign of the two different clinical conditions. A better state of consciousness is often associated with increased activity in the anterior (Jang & Kwon, 2019; Toppi et al., 2024), and our findings provide supporting evidence for this association. We also analyzed the differences in PSD and SCCM-based brain networks between anterior and posterior brain regions, and found no significant differences between the two patient groups across all frequency bands.

To address potential gender-related confounding, we conducted a supplementary sub-analysis using a gender-matched subset of patients (16 males and 16 females). This analysis was repeated three times with different random selections of male patients to ensure robustness. Across all repetitions, the results (Fig. S3 and S4 in supplementary material) consistently confirmed our main findings: significant group differences were observed in LR within the α band, in the relative LR in α band and δ band, and in AP within the θ band. These findings indicate that the observed network alterations are robust and not driven by gender distribution in the cohort.

For further comparison, we also evaluated conventional electrode coupling measures (symbolic transfer entropy, phase transfer entropy, coherence, Phase-Locking Value, and weighted Phase Lag Index) on the DOC dataset. None of these methods revealed significant LR or AP asymmetry differences between the two patient groups. These results are provided in the supplementary material (Fig. S5-S8 in the supplementary material).

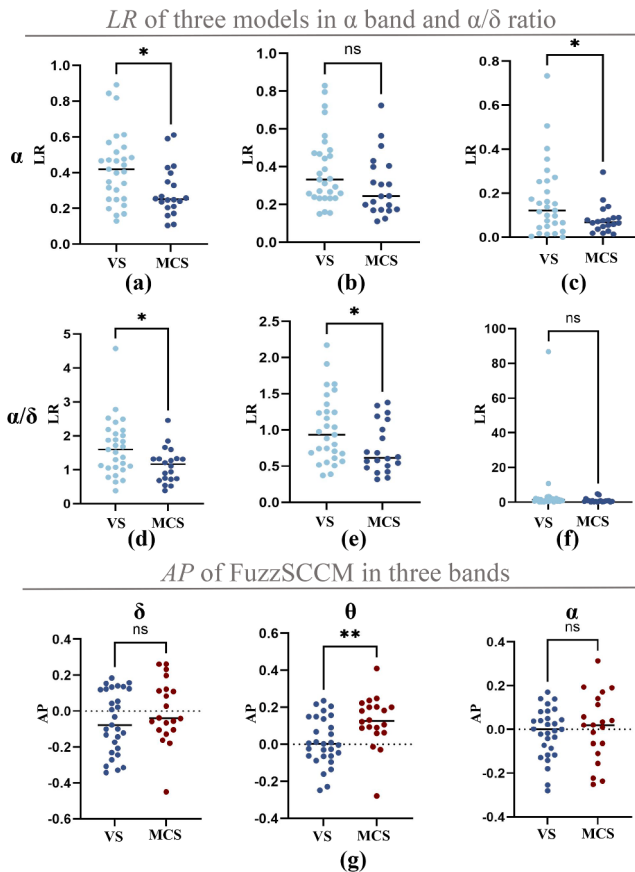


Fig. 5. Comparison of brain network features between VS and MCS patients across different methods. (a-c) LR values in the α band derived from FuzzSCCM, SCCM, and PSD, respectively. (d-f) Relative LR in α band and δ band obtained from FuzzSCCM, SCCM, and PSD, respectively. (g) AP values of FuzzSCCM in the δ , θ , and α bands. Unpaired t-test was performed, * $p < 0.05$, ** $p < 0.01$.

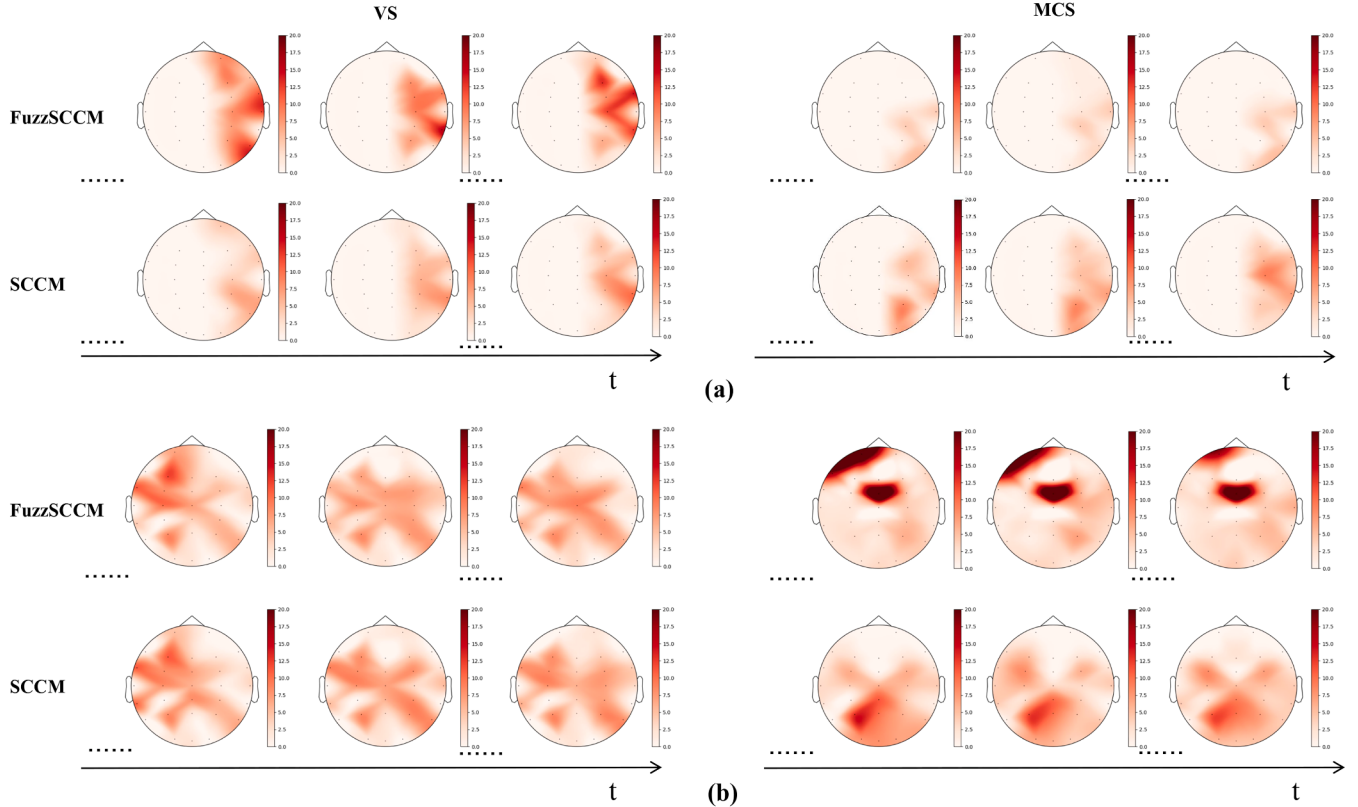


Fig. 6. Comparison of degree distributions obtained by FuzzSCCM and SCCM in representative patients. FuzzSCCM successfully captures distinct asymmetries between VS and MCS patients, whereas SCCM fails to reveal clear differences. (a) Left-right hemispheric degree differences. (b) Whole-brain degree distributions.

For the stroke dataset, given that stroke lesions are often associated with hemispheric asymmetry, we employed the LR metric to assess whether this asymmetry could be detected in the constructed brain networks. Specifically, we compared LR values in the δ , θ , and α bands. The results (Fig.S9 in supplementary material) showed significant differences ($p < 0.05$) between stroke patients and healthy controls across all three frequency bands, indicating that our method is capable of capturing hemispheric imbalance in an independent dataset. These findings provide empirical evidence that the proposed FuzzSCCM is not limited to DOC but can be generalized to other neurological conditions.

Since electrode coupling in patients is not static, we employed NMF and Markov chain modeling to capture the dynamic coupling relationships between electrodes over time. The details can be found in Section 2.4. The value of N_{co} is considered reasonable between 7 and 14 (Tangwiriyasakul et al., 2018). To evaluate this, the selection criteria of N_{co} is as follows:

We focused on the independence among components rather than the absolute values of matrix elements. To assess independence, we calculated the PCC between components under different N_{co} . As shown in Fig. 7(a), the pairwise correlations, and in Fig. 7(b), the mean correlation values, both demonstrate that independence among components is maximized when $N_{co} = 12$. And Bayesian Information Criterion (BIC) analysis (Fig. 7(c)) indicated that $N_{co} = 12$ provided the best trade-off between model fit and complexity. Finally, we compared the average PCC between FC matrices of each patient and the generated sub-networks under different values of N_{co} in α band. As shown in Fig. 7(d), no significant differences were observed across patients when the number of components was set to 12 or 14, but both values were higher than that obtained at $N_{co} = 10$. Therefore, selecting 12 components not only maintains performance but also conserves computational resources.

Each brain network was mapped to the specific sub-network with the highest PCC among the 12 sub-networks. The time-dependent char-

acteristics of brain networks were preserved, allowing us to capture brain dynamics through the resulting network sequence. The initial step is to investigate whether 12 sub-networks show significant differences ($p < 0.05$) in occurrence probability across the two patient groups. The occurrence probability of a sub-network was defined as the ratio of its number of occurrences to the total number of windows (30). Building upon this finding, we investigated differences in transition probabilities from the discrepant sub-networks to other brain networks in VS and MCS patients. Then we treat the brain network sequence as a Markov chain and compute the one-step transition probability of the brain network. The transition probability is approximated using observed data. The process is as follows.

$$P_{ij} = P(X_{n+1} = j | X_n = i) \approx C_{ij}/C_i \quad (25)$$

Let X_n denotes the specific sub-network state of the n th window, where P_{ij} represents the probability of migrating from state i to state j . Here, C_{ij} is the number of transitions from state i to state j , and C_i is the total number of occurrences of state i . Each subject has a state sequence of length 30, from which the one-step transition probability is computed.

In the low-frequency bands, no significant difference was found in the transition probability and occurrence probability between the two types of groups. We therefore focused on the α frequency band and compared all transition probabilities between VS and MCS patients (Fig. 1(c)). To address the issue of multiple comparisons, statistical results were corrected using the Bonferroni correction (family-wise error rate, FWE correction). In the α band, a significant difference ($p < 0.05$) in the occurrence probability of sub-network 10 was observed between the MCS and VS groups. From Fig. 8(e), an obvious difference ($p < 0.05$, FWE corrected) was observed in the transition from sub-network 10 ($LR = 0.10$) to sub-network 8 ($LR = 0.02$). Analyzing the out-degree and in-degree, we found that the asymmetry between the left and right

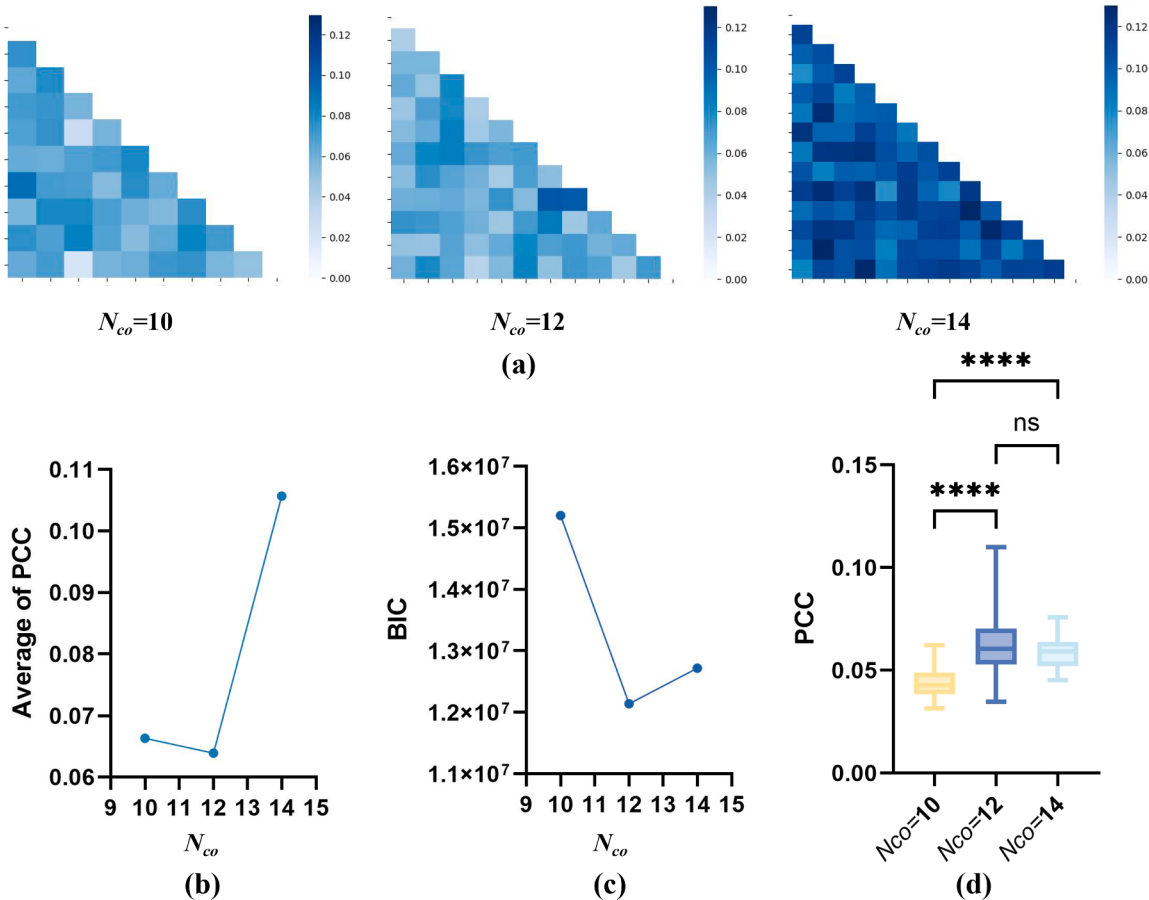


Fig. 7. Selection of the optimal number of components (N_{co}). (a) Pairwise PCCs between components estimated with different values of N_{co} . (b) Mean PCCs across all component pairs, illustrating the overall independence of components at each N_{co} . (c) BIC values for different N_{co} . (d) The mean value of the Pearson correlation coefficient between all the FC matrices of the subjects and the matched sub-networks. Unpaired t-test was performed. *** $p < 0.0001$.

hemispheres was more pronounced in sub-network 10 than in sub-network 8 (Fig. 8(a-d)). These findings suggest that MCS patients exhibit left-right hemispheric oscillation asymmetry for a certain period but have a higher probability of transition to a more symmetrical state. This transition may be a crucial factor in achieving a better clinical condition. Our approach provides new evidence from a dynamic perspective.

5. Discussion

In this study, we introduced FuzzSCCM, an extension of convergent cross mapping that incorporates fuzzy membership functions. Additionally, we applied FuzzSCCM to analyze electrode coupling in patients with DOC. By leveraging symbolic pattern analysis, FuzzSCCM effectively captures various types of causal relationships. To account for temporal variations in real systems, we incorporated a Bayesian NMF approach to estimate the causal dynamics. We validated the method's performance using simulation data and compared it with other convergent cross-mapping-based techniques. The simulation results demonstrated that FuzzSCCM was sensitive to the coupling strength but robust to variations in data length. Moreover, FuzzSCCM exhibits superior adaptability in detecting coupling within weakly coupled systems and systems affected by complex noise.

Similar to the SCCM method, FuzzSCCM does not analyze raw time series directly, but instead focuses on symbolic patterns. However, unlike SCCM, which emphasizes dispersion modes, FuzzSCCM primarily captures fluctuation in data. With respect to why the FuzzSCCM is not

sensitive to the noise, this may be related to the introduction of the fuzzy membership function. After estimating symbolic patterns from the original time series, we apply fuzzy membership functions to expand the symbols to fuzzy symbols. Since noise-induced fluctuations can significantly alter discrete symbols, our approach mitigates this issue by expanding symbols into fuzzy representations, thereby reducing the impact of noise perturbations. In addition, the simulation results showed that symbolic methods were also not sensitive to data length. This may be because the fluctuation of data is more stable than the values of data in a certain system.

Furthermore, FuzzSCCM was used to examine electrode coupling in DOC patients across three frequency bands. Our investigation was composed of static and dynamic functional network properties derived from resting-state EEG data. Specifically, we computed causal relationships between electrodes and constructed functional brain networks based on these causal relationships. To identify potential biomarkers associated with better clinical outcomes, we analyzed the frequency bands in which significant differences were observed.

Patients exhibiting higher levels of consciousness demonstrated significantly stronger functional connectivity among brain regions (Hannawi et al., 2015). The prefrontal cortex plays a key role in the formation of consciousness (Laureys, 2005). To assess the difference in connectivity between anterior and posterior regions, we calculated AP. As shown in Fig. 5(d), MCS patients had a much higher AP in the θ band. This finding suggests that the frontal regions are more active than the parietal regions in MCS patients, particularly in the θ band, which may be an important factor affecting the state of consciousness. Notably, this

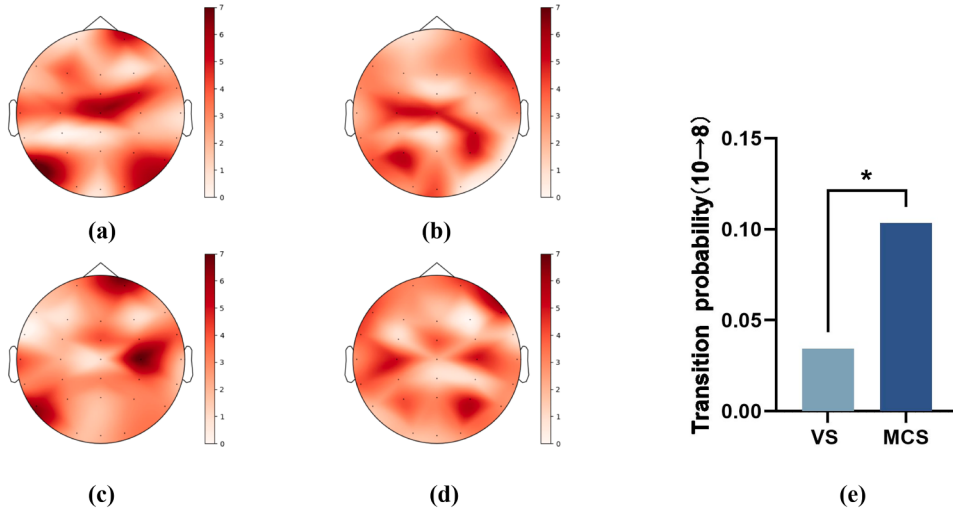


Fig. 8. In-degree and out-degree of sub-networks 8 and 10 in α band. A significant difference in the transition probability from sub-network 10 to sub-network 8 was observed between the two patient groups. (a-b)Out-degree of sub-network 10 and 8. (c-d)In-degree (bottom) of sub-network 8. (e)Comparison of transition probabilities between VS and MCS patients. Bars represent median values for each group(Unpaired t-test was performed, * $p < 0.05$, FWE corrected).

anterior-posterior differentiation was entirely undetected by traditional methods, underscoring the superior sensitivity of our proposed approach in identifying subtle yet clinically meaningful connectivity patterns.

In addition, our analysis revealed that our sample of VS patients showed significantly higher asymmetry of left and right hemisphere connections estimated in the EEG high-frequency oscillation, and this finding aligns with PSD results. We hypothesize that this asymmetry may be attributed to the fact that the α power of VS patients is much lower than that of MCS (Lehembre et al., 2012; Stefan et al., 2018). Importantly, this effect was not detected by previous methods, highlighting the superior sensitivity of FuzzSCCM in capturing clinically relevant hemispheric differences. Furthermore, relative asymmetry in the α/δ ratio also showed significant group-level differences between VS and MCS patients. Taken together, these findings suggest that reduced hemispheric asymmetry may serve as a potential biomarker for distinguishing clinical states of consciousness, with FuzzSCCM providing a more robust detection framework than traditional methods.

In terms of computational efficiency, processing a sample with a length of 1000 requires approximately one minute on standard hardware (Intel i7 CPU, 16 GB RAM), without the need for specialized computing resources. This relatively low computational cost suggests that FuzzSCCM is not only suitable for offline analysis but also holds potential for near real-time monitoring of brain network dynamics in clinical practice.

An important consideration for the clinical application of our proposed method is its generalizability across different patient populations. While our primary analyses focused on DOC patients, we further tested the applicability of FuzzSCCM in a cohort of stroke patients. Since stroke lesions often induce structural and functional asymmetries across hemispheres, this population provides an appropriate testbed for validating whether our method and the derived LR metric can capture clinically meaningful network alterations. Given the exploratory nature of this analysis, we limited our comparison to the LR metric in the δ , θ , and α frequency bands. The results revealed significant differences in hemispheric asymmetry between stroke patients and healthy controls across these bands. This finding suggests that FuzzSCCM can reliably detect network-level asymmetries beyond DOC, thereby supporting its broader clinical applicability as an auxiliary diagnostic tool. In the future, we will further validate FuzzSCCM on larger, multicenter clinical datasets to enhance its reliability and translational potential in clinical practice.

In a dynamic perspective, we first used Bayesian NMF to obtain 12 sub-networks in three frequency bands. Then, all patients' brain net-

work sequences were mapped into sub-network sequences obtained by the above steps. Then, we modeled the entire sequence of each patient as a Markov chain to calculate the one-step transition probability between sub-networks. Before calculating transition probabilities, we first examined the occurrence frequency of each sub-network in the two groups. This analysis revealed that sub-network 10 in α band appeared with significantly different probabilities between MCS and VS patients. Guided by this finding, we then focused on the transition dynamics originating from sub-network 10. Fig. 8 illustrates the sub-networks with significantly different transition probabilities between VS and MCS patients in the α band. Among them, the transfer probability from sub-network 10 to sub-network 8 was significantly higher in MCS patients than in VS patients. To further investigate these differences, we briefly analyzed the out-degree and in-degree of the two sub-networks. Compared with sub-network 8, the out-degree asymmetry of sub-network 10 is more serious. According to the results, we find that, in the dynamic evolution of brain networks, MCS patients have a higher probability of transitioning from an asymmetric state to a more symmetric state in the left and right hemispheres. These results highlight that FuzzSCCM not only sensitively captures coupling strength but also effectively characterizes dynamic variations in brain connectivity across time windows, suggesting that dynamic network transitions may serve as an additional biomarker for differentiating clinical states of consciousness.

This study both complements previous literature and establishes a novel framework for investigating the brain architecture of DOC patients. Although FuzzSCCM provides a robust framework for quantifying directed coupling, an inherent limitation of the current study is that the method is applied in a pairwise manner. This restriction is shared by many classical approaches, such as Granger causality, transfer entropy, and symbolic methods, where pairwise interactions serve as the basis for constructing large-scale brain networks. Recognizing this limitation, we will next expand it to multivariate situations. In the future, we will adopt conditional causality analysis, where the influence between two electrodes is evaluated while statistically controlling for the activity of other nodes, thereby reducing spurious pairwise effects.

6. Conclusion

For the first time, we proposed a symbolic convergent cross-mapping method incorporating a fuzzy membership function for comprehensive analysis of cross-signal coupling. Simulation results demonstrated that the FuzzSCCM method outperformed two CCM methods, exhibiting

sensitivity to coupling strength while remaining robust to data length and noise. Further analysis of experimental EEG data revealed that the left-right hemispheric connectivity asymmetry of MCS patients was weaker in α band, and MCS patients had a significantly higher AP in θ band. Importantly, these clinically relevant differences were uniquely detected by FuzzSCCM and were not captured by traditional CCM-based methods, underscoring the enhanced sensitivity of our approach. We further evaluated the proposed method on a larger EEG dataset from stroke patients, and the consistent performance demonstrates its robustness and broader applicability.

Additionally, we used Bayesian NMF to capture the dynamic properties of brain networks in DOC patients. The results showed that the one-step transition probabilities between specific sub-networks were significantly different between the two clinical conditions. This makes it a promising tool to assist clinicians in differentiating levels of consciousness in DOC patients. By capturing subtle differences in dynamic network interactions, FuzzSCCM may provide objective neurophysiological markers that complement behavioral assessments. Nevertheless, we acknowledge that the current implementation is limited to bivariate analyses and further validation on larger datasets is still required. In future work, we plan to extend FuzzSCCM to multivariate analyses and perform comprehensive validation using larger, multicenter cohorts to further improve its generalizability and clinical relevance.

CRediT authorship contribution statement

Tingting Li: Writing – original draft, Software, Methodology, Conceptualization; **Xingwei An:** Writing – review & editing, Supervision; **Yang Di:** Methodology, Data curation, Conceptualization; **Honglin Wang:** Data curation; **Yujia Yan:** Data curation; **Shuang Liu:** Supervision; **Yueqing Dong:** Data curation; **Dong Ming:** Supervision.

Data availability

The authors do not have permission to share data. The code is available at <https://github.com/Medbcf/FuzzSCCM>

Declaration of competing interest

None.

Acknowledgments

This work was supported in part by funding from the Science and Technology Innovation 2030-Major Project (No. 2022ZD0208500), and the National Natural Science Foundation of China (No. 62276181).

Supplementary material

Supplementary material associated with this article can be found in the online version at [10.1016/j.neunet.2025.108318](https://doi.org/10.1016/j.neunet.2025.108318)

References

- Abuhasel, K. A., Iliyasu, A. M., & Faticah, C. (2015). A hybrid particle swarm optimization and neural network with fuzzy membership function technique for epileptic seizure classification. *Journal of Advanced Computational Intelligence and Intelligent Informatics*, 19(3), 447–455.
- Bai, Y., Yang, L., Meng, X., Huang, Y., Wang, Q., Gong, A., Feng, Z., & Ziemann, U. (2024). Breakdown of effective information flow in disorders of consciousness: Insights from TMS-EEG. *Brain Stimulation*, 17(3), 533–542.
- Ballanti, S., Campagnini, S., Lituzzi, P., Hakiki, B., Scarpino, M., Macchi, C., Oddo, C. M., Carrozza, M. C., Grippo, A., & Mannini, A. (2022). EEG-based methods for recovery prognosis of patients with disorders of consciousness: A systematic review. *Clinical Neurophysiology*, 144, 98–114.
- Cao, J., Zhao, Y., Shan, X., Wei, H.-l., Guo, Y., Chen, L., Erkoyuncu, J. A., & Sarrigiannis, P. G. (2022). Brain functional and effective connectivity based on electroencephalography recordings: A review. *Human Brain Mapping*, 43(2), 860–879.
- Chatterjee, D., Sinharay, A., & Konar, A. (2013). EEG-based fuzzy cognitive load classification during logical analysis of program segments. In *2013 IEEE International conference on fuzzy systems (FUZZ-IEEE)* (pp. 1–6). IEEE.
- Chen, X., Zhang, Y., Cheng, S., & Xie, P. (2019). Transfer spectral entropy and application to functional corticomuscular coupling. *IEEE Transactions on Neural Systems and Rehabilitation Engineering*, 27(5), 1092–1102.
- Chennu, S., Annen, J., Wannez, S., Thibaut, A., Chatelle, C., Cassol, H., Martens, G., Schnakers, C., Gosseries, O., Menon, D., Laureys, S. (2017). Brain networks predict metabolism, diagnosis and prognosis at the bedside in disorders of consciousness. *Brain*, 140(8), 2120–2132.
- David, O., Cosmelli, D., & Friston, K. J. (2004). Evaluation of different measures of functional connectivity using a neural mass model. *Neuroimage*, 21(2), 659–673.
- Demertzis, A., Tagliazucchi, E., Dehaene, S., Deco, G., Barttfeld, P., Raimondo, F., Martial, C., Fernández-Espejo, D., Rohaut, B., Voss, H. U., Schiff, N. D., Owen, A. M., Laureys, S., Naccache, N., Sitt, J. D., (2019). Human consciousness is supported by dynamic complex patterns of brain signal coordination. *Science Advances*, 5(2), eaat7603.
- Dhamala, M., Rangarajan, G., & Ding, M. (2008). Analyzing information flow in brain networks with nonparametric Granger causality. *Neuroimage*, 41(2), 354–362.
- Faes, L., Nollo, G., & Porta, A. (2011). Information-based detection of nonlinear Granger causality in multivariate processes via a nonuniform embedding technique. *Physical Review E-Statistical, Nonlinear, and Soft Matter Physics*, 83(5), 051112.
- Geweke, J. (1982). Measurement of linear dependence and feedback between multiple time series. *Journal of the American Statistical Association*, 77(378), 304–313.
- Geweke, J. F. (1984). Measures of conditional linear dependence and feedback between time series. *Journal of the American Statistical Association*, 79(388), 907–915.
- Giacino, J. T., Kalmar, K., & Whyte, J. (2004). The JFK coma recovery scale-revised: Measurement characteristics and diagnostic utility. *Archives of Physical Medicine and Rehabilitation*, 85(12), 2020–2029.
- Giacino, J. T., Katz, D. I., Schiff, N. D., Whyte, J., Ashman, T. J., Ashwal, S., Barbano, R., Hammond, F. M., Laureys, S., Ling, G. S. F., Nakase-Richardson, R., Seel, R. T., Yablon, S. A., Getchius, T. S. D., Gronseth, G. S., Armstrong, M. J., (2018). Comprehensive systematic review update summary: disorders of consciousness: Report of the guideline development, dissemination, and implementation subcommittee of the American academy of neurology; the American congress of rehabilitation medicine; and the national institute on disability, independent living, and rehabilitation research. *Neurology*, 91(10), 461–470.
- Granger, C. W. J. (1969). Investigating causal relations by econometric models and cross-spectral methods. *Econometrica: Journal of the Econometric Society*, 37, (pp. 424–438).
- Gu, D., Lin, A., & Lin, G. (2023). Detection of attention deficit hyperactivity disorder in children using CEEMDAN-based cross frequency symbolic convergent cross mapping. *Expert Systems with Applications*, 226, 120105.
- Hannawi, Y., Lindquist, M. A., Caffo, B. S., Sair, H. I., & Stevens, R. D. (2015). Resting brain activity in disorders of consciousness: A systematic review and meta-analysis. *Neurology*, 84(12), 1272–1280.
- Hao, Z., Xia, X., Pan, Y., Bai, Y., Wang, Y., Peng, B., & Dou, W. (2023). Uncovering brain network insights for prognosis in disorders of consciousness: EEG source space analysis and brain dynamics. *IEEE Transactions on Neural Systems and Rehabilitation Engineering*, 32, 144–153.
- Jang, S. H., & Kwon, Y. H. (2019). Neuroimaging characterization of recovery of impaired consciousness in patients with disorders of consciousness. *Neural Regeneration Research*, 14(7), 1202–1207.
- Jansen, B. H., & Rit, V. G. (1995). Electroencephalogram and visual evoked potential generation in a mathematical model of coupled cortical columns. *Biological Cybernetics*, 73(4), 357–366.
- King, J.-R., Sitt, J. D., Faugeras, F., Rohaut, B., El Karoui, I., Cohen, L., Naccache, L., & Dehaene, S. (2013). Information sharing in the brain indexes consciousness in non-communicative patients. *Current Biology*, 23(19), 1914–1919.
- Kondziella, D., Friberg, C. K., Frokjaer, V. G., Fabricius, M., & Möller, K. (2016). Preserved consciousness in vegetative and minimal conscious states: Systematic review and meta-analysis. *Journal of Neurology, Neurosurgery & Psychiatry*, 87(5), 485–492.
- Laureys, S. (2005). The neural correlate of (un) awareness: Lessons from the vegetative state. *Trends in Cognitive Sciences*, 9(12), 556–559.
- Lazar, P., Jayapathy, R., Torrents-Barrena, J., Mol, B., Mohanalin, & Puig, D. (2016). Fuzzy-entropy threshold based on a complex wavelet denoising technique to diagnose Alzheimer disease. *Healthcare Technology Letters*, 3(3), 230–238.
- Lehembre, R., Bruno, M.-A., Vanhaudenhuyse, A., Chatelle, C., Cologan, V., Leclercq, Y., Soddu, A., Macq, B., Laureys, S., & Noirhomme, Q. (2012). Resting-state EEG study of comatoses patients: A connectivity and frequency analysis to find differences between vegetative and minimally conscious states. *Functional Neurology*, 27(1), 41.
- Lungarella, M., Pitti, A., & Kuniyoshi, Y. (2007). Information transfer at multiple scales. *Physical Review E-Statistical, Nonlinear, and Soft Matter Physics*, 76(5), 056117.
- Mi, Y., & Lin, A. (2024). Spectral time-varying pattern causality and its application. *IEEE Journal of Biomedical and Health Informatics*. 28, 3742–3749.
- Rizkallah, J., Annen, J., Modolo, J., Gosseries, O., Benquet, P., Mortahab, S., Amoud, H., Cassol, H., Mheich, A., Thibaut, A., Chatelle, C., Hassan, M., Panda, R., Wendling, F., Laureys, S., (2019). Decreased integration of EEG source-space networks in disorders of consciousness. *NeuroImage: Clinical*, 23, 101841.
- Rostaghi, M., Khatibi, M. M., Ashory, M. R., & Azami, H. (2021). Fuzzy dispersion entropy: A nonlinear measure for signal analysis. *IEEE Transactions on Fuzzy Systems*, 30(9), 3785–3796.
- Schmidt, M. N., Winther, O., & Hansen, L. K. (2009). Bayesian non-negative matrix factorization. In *International conference on independent component analysis and signal separation* (pp. 540–547). Springer.
- Schnakers, C., Vanhaudenhuyse, A., Giacino, J., Ventura, M., Boly, M., Majerus, S., Moonen, G., & Laureys, S. (2009). Diagnostic accuracy of the vegetative and minimally

- conscious state: Clinical consensus versus standardized neurobehavioral assessment. *BMC Neurology*, 9, 1–5.
- Schreiber, T. (2000). Measuring information transfer. *Physical Review Letters*, 85(2), 461.
- Stavroglou, S. K., Pantelous, A. A., Stanley, H. E., & Zuev, K. M. (2019). Hidden interactions in financial markets. *Proceedings of the National Academy of Sciences*, 116(22), 10646–10651.
- Stefan, S., Schorr, B., Lopez-Rolon, A., Kolassa, I.-T., Shock, J. P., Rosenfelder, M., Heck, S., & Bender, A. (2018). Consciousness indexing and outcome prediction with resting-state EEG in severe disorders of consciousness. *Brain Topography*, 31, 848–862.
- Sugihara, G., May, R., Ye, H., Hsieh, C.-h., Deyle, E., Fogarty, M., & Munch, S. (2012). Detecting causality in complex ecosystems. *Science*, 338(6106), 496–500.
- Tangwiriyasakul, C., Perani, S., Centeno, M., Yaakub, S. N., Abela, E., Carmichael, D. W., & Richardson, M. P. (2018). Dynamic brain network states in human generalized spike-wave discharges. *Brain*, 141(10), 2981–2994.
- Toppi, J., Quattrociocchi, I., Riccio, A., D'Ippolito, M., Aloisi, M., Colamarino, E., Pichiorri, F., Cincotti, F., Formisano, R., & Mattia, D. (2024). EEG-derived markers to improve prognostic evaluation of disorders of consciousness. *IEEE Journal of Biomedical and Health Informatics*, 28, 6674–6684.
- Vlachos, I., & Kugiumtzis, D. (2010). Nonuniform state-space reconstruction and coupling detection. *Physical Review E-Statistical, Nonlinear, and Soft Matter Physics*, 82(1), 016207.
- Wang, J., Zhao, S., Xu, C., Zhang, J., & Zhong, R. (2022). Brain-inspired interpretable network pruning for smart vision-based defect detection equipment. *IEEE Transactions on Industrial Informatics*, 19(2), 1666–1673.
- Yan, Y., An, X., Ren, H., Luo, B., Jin, S., Liu, L., Di, Y., Li, T., & Huang, Y. (2024). Nomogram-based geometric and hemodynamic parameters for predicting the growth of small untreated intracranial aneurysms. *Neurosurgical Review*, 47(1), 169.
- Yi, C., Chen, C., Si, Y., Li, F., Zhang, T., Liao, Y., Jiang, Y., Yao, D., & Xu, P. (2020). Constructing large-scale cortical brain networks from scalp EEG with Bayesian non-negative matrix factorization. *Neural Networks*, 125, 338–348.
- Yi, C., Qiu, Y., Chen, W., Chen, C., Wang, Y., Li, P., Yang, L., Zhang, X., Jiang, L., Yao, D., et al. (2022). Constructing time-varying directed EEG network by multivariate non-parametric dynamical Granger causality. *IEEE Transactions on Neural Systems and Rehabilitation Engineering*, 30, 1412–1421.
- Zhang, Y., & Chen, Z. S. (2025). Harnessing electroencephalography connectomes for cognitive and clinical neuroscience. *Nature Biomedical Engineering*, 9, (pp. 1–16).